Available online at www.sciencedirect.com

ScienceDirect

Geochimica et Cosmochimica Acta 124 (2014) 223–236

Geochimica et Cosmochimica Acta

www.elsevier.com/locate/gca

Stable isotope time-series in mammalian teeth: *In situ* $\delta^{18}O$ from the innermost enamel layer

Scott A. Blumenthal [a,b,*], Thure E. Cerling [c,d], Kendra L. Chritz [c], Timothy G. Bromage [e,f], Reinhard Kozdon [g], John W. Valley [g]

[a] *Department of Anthropology, The Graduate Center, City University of New York, New York, NY 10016, USA*
[b] *The New York Consortium in Evolutionary Primatology (NYCEP), New York, NY 10016, USA*
[c] *Department of Biology, University of Utah, Salt Lake City, UT 84112, USA*
[d] *Department of Geology and Geophysics, University of Utah, Salt Lake City, UT 84112, USA*
[e] *Department of Biomaterials & Biomimetics, New York University College of Dentistry, New York, NY 10010, USA*
[f] *Department of Basic Science & Craniofacial Biology, New York University College of Dentistry, New York, NY 10010, USA*
[g] *WiscSIMS, Department of Geoscience, University of Wisconsin-Madison, WI 53705, USA*

Received 15 April 2013; accepted in revised form 22 September 2013; Available online 8 October 2013

Abstract

Stable carbon and oxygen isotope ratios in mammalian tooth enamel are commonly used to understand the diets and environments of modern and fossil animals. Isotope variation during the period of enamel formation can be recovered by intra-tooth microsampling along the direction of growth. However, conventional sampling of the enamel surface provides highly time-averaged records in part due to amelogenesis. We use backscattered electron imaging in the scanning electron microscope (BSE-SEM) to evaluate enamel mineralization in developing teeth from one rodent and two ungulates. Gray levels from BSE-SEM images suggest that the innermost enamel layer, <20 μm from the enamel–dentine junction, is highly mineralized early in enamel maturation and therefore may record a less attenuated isotopic signal than other layers. We sampled the right maxillary incisor from a woodrat subjected to an experimentally induced water-switch during the period of tooth development, and demonstrate that secondary ion mass spectrometry (SIMS) can be used to obtain $\delta^{18}O$ values with 4–5-μm spots from mammalian tooth enamel. We also demonstrate that SIMS can be used to discretely sample the innermost enamel layer, which is too narrow for conventional microdrilling or laser ablation. An abrupt $\delta^{18}O$ switch of 16.0‰ was captured in breath CO_2, a proxy for body water, while a laser ablation enamel surface intra-tooth profile of the left incisor captured a $\delta^{18}O$ range of 12.1‰. The innermost enamel profile captured a $\delta^{18}O$ range of 15.7‰, which approaches the full magnitude of $\delta^{18}O$ variation in the input signal. This approach will likely be most beneficial in taxa such as large mammalian herbivores, whose teeth are characterized by less rapid mineralization and therefore greater attenuation of the enamel isotope signal.

1. INTRODUCTION

Stable isotope analysis of mammalian calcified tissues is commonly used in geological, biological, and archaeological research, and is a powerful geochemical tool for reconstructing short-term variability in the diets and environments of modern and fossil animals. Stable isotope ratios of carbon ($\delta^{13}C$) are related to the animal's food source

* Corresponding author at: Department of Anthropology, The Graduate Center, City University of New York, New York, NY 10016, USA. Tel.: +1 224 637 0762.
E-mail address: blumenthal.scott@gmail.com (S.A. Blumenthal).

0016-7037/$ - see front matter © 2013 Elsevier Ltd. All rights reserved.
http://dx.doi.org/10.1016/j.gca.2013.09.032

(DeNiro and Epstein, 1978; Cerling and Harris, 1999). Stable isotope ratios of oxygen ($\delta^{18}O$) are related to available water, mediated by physiology and drinking behavior, as body water is a function of meteoric water ingested directly by drinking and indirectly through water in food and inspired air (Longinelli, 1984; Luz et al., 1984; Bryant and Froelich, 1995; Kohn et al., 1996; Podlesak et al., 2008). Isotope time-series within the lifetimes of individual animals can be recovered from incrementally growing tissues that do not remodel after formation, such as dental tissues. Intra-tooth microsampling was first demonstrated using dentine (Koch et al., 1989), which preserves a high resolution record of isotopic variability (Zazzo et al., 2006; Kirsanow et al., 2008; Codron et al., 2012). However, tooth enamel is more resistant to diagenetic alteration than is dentine; therefore it is more reliable for paleobiological and paleoecological applications (Ayliffe et al., 1994; Koch et al., 1997; Zazzo et al., 2004). Variability in enamel isotope values within a tooth row (Bryant et al., 1996a; Fricke and O'Neil, 1996) and within a single tooth (Fricke and O'Neil, 1996; Kohn et al., 1998; Sharp and Cerling, 1998) record a chronological record of dietary and environmental input throughout the period of enamel formation, which among mammals ranges from weeks to years (Balasse, 2002; Kohn, 2004). Following this approach, intra-tooth variability in enamel $\delta^{13}C$ and $\delta^{18}O$ values from modern and fossil animals has been used to address a wide range of problems requiring intra-annual time resolution, including seasonality of animal diet (Balasse, 2002; Fox and Fisher, 2004; Zazzo et al., 2010; Metcalfe and Longstaffe, 2012), migration (Britton et al., 2009; Julien et al., 2012), and birth (Balasse et al., 2003, 2011; Chritz et al., 2009; Frémondeau et al., 2012), as well as climate seasonality (Fricke et al., 1998; Kohn et al., 1998, 2002; Sharp and Cerling, 1998; Fox and Fisher, 2001; Nelson, 2005; Bernard et al., 2009; Higgins and Macfadden, 2009; Stevens et al., 2011; Brookman and Ambrose, 2012; Hallin et al., 2012) and movement patterns of prehistoric human populations (Balasse et al., 2002).

Tooth enamel is a calcium phosphate bioapatite approximating hydroxyapatite $Ca_{10}(PO_4)_6(OH)_2$ (Elliott, 2002). Structural carbonate (CO_3) groups are present as a substitute for the phosphate (ca. 90%) and hydroxyl groups (ca. 10%) (LeGeros et al., 1969; Elliott et al., 1985; Shi et al., 2005). Mature enamel is highly mineralized, approximately 95–98% by weight, with the remaining components composed of organic matter and water (Glick, 1979; Elliott, 1997; Smith, 1998). Total water content includes the sum of H_2O in the organic phase, evolved at low temperatures (approximately 110 °C), and constitutional H_2O of the apatite phase, which is stable to approximately 1400 °C (Elliott, 1997). Oxygen in enamel bioapatite is present in the PO_4, CO_3, and OH^-groups, with oxygen contents of 35%, 3.3%, and 1.6%, respectively (Cerling and Sharp, 1996). Each component of tooth enamel with oxygen has a different fractionation from body water. Enamel phosphate and carbonate precipitate in equilibrium with each other, with a fractionation of approximately 9‰ between oxygen in PO_4 (depleted) and CO_3 (enriched) (Bryant et al., 1996a,b; Cerling and Sharp, 1996; Iacumin et al., 1996; Pellegrini et al., 2011). The $\delta^{18}O$ fractionation between OH^- and PO_4 has been estimated indirectly to be −16.6‰ (Jones et al., 1999). Therefore, analyses of different reservoirs of oxygen in tooth enamel are expected to provide different $\delta^{18}O$ values, with total oxygen *in situ* analysis representing bulk enamel assuming complete mixing. The value for $^{18}\varepsilon^*_{\text{bulk-carbonate}}$ is predicted to range between −8‰ and −9‰, assuming some variability in CO_3 content and more positive actual fractionation between OH^- and PO_4 (Passey and Cerling, 2006). The more positive measured enrichment values for modern enamel that range between −5.3‰ and −7.6‰ may reflect incomplete mixing of oxygen-bearing phases during *in situ* laser ablation and a bias towards oxygen in CO_3 (Passey and Cerling, 2006; Podlesak et al., 2008).

Enamel development (amelogenesis) is a multi-stage process that starts with the deposition of an organic-rich primary matrix and the appearance of incremental growth features, which is followed by a prolonged period of maturation associated with widening and thickening of bioapatite crystals, the progressive removal of proteins and pore fluid, and increasing mineralization (Allan, 1967; Suga et al., 1970; Sakae and Hirai, 1982; Suga, 1982, 1983; Robinson et al., 1995; Moss-Salentijn et al., 1997). Mineralization is a spatially diffuse process, with multiple maturation fronts following trajectories throughout the enamel layer that do not all align with the incremental growth lines (Allan, 1967; Suga, 1979, 1982; Tafforeau et al., 2007). Therefore, these lines are a poor guide for understanding isotope incorporation that occurs during the enamel maturation stage and causes significant signal attenuation in intra-tooth isotope profiles (Fisher and Fox, 1998; Passey and Cerling, 2002; Balasse, 2003; Hoppe et al., 2004). Conventionally, enamel has been sampled sequentially with a drill or laser perpendicular to the growth axis. Typically sampling extends partially or entirely through the thickness of enamel, which introduces additional time-averaging by integrating enamel from distinct appositional growth and mineralization intervals (Passey and Cerling, 2002; Balasse, 2003; Hoppe et al., 2004; Zazzo et al., 2005). Therefore, individual intra-tooth samples do not represent discrete intervals of time, and establishing a precise chronology is often difficult. Blurred intra-tooth isotope profiles are characterized by the loss of both signal amplitude and structure, such that sinusoidal and non-sinusoidal signals may be indistinguishable, or at least significantly modified.

A forward model has been developed describing isotope signal time-averaging in enamel intra-tooth profiles (Passey and Cerling, 2002). Model parameters (Fig. 1) include initial mineral content of deposited enamel (f_i), increase in enamel thickness over constant length of apposition (l_a) (corresponding to the matrix deposition stage of amelogenesis), linear increase in mineralization over constant length of maturation (corresponding to the maturation stage of amelogenesis) (l_m), and a constant growth rate such that length along the tooth also reflects time. The model for signal attenuation during amelogenesis can be expressed mathematically as:

$$\delta_{ei} = (f_i * \delta_{mi}) + (1 - f_i) * \frac{\sum_{n=i+1}^{i+1+l_m} \delta_{m_n}}{l_m} \quad (1)$$

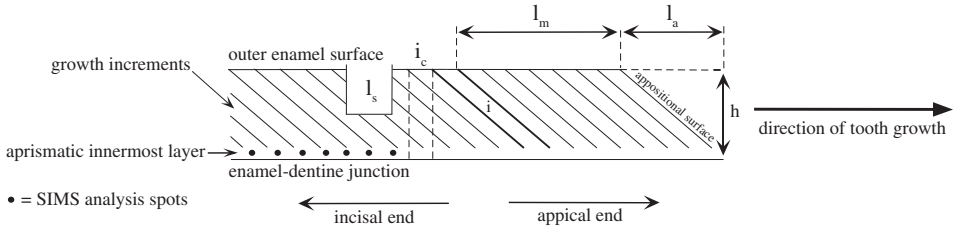

Fig. 1. Schematic diagram of enamel maturation parameters. The length of apposition l_a is the length over which the highly organic initial matrix is deposited, or the distance from where the appositional layer contacts the enamel-dentine junction to where it contacts the outer surface; the length of maturation l_m is the length over which enamel mineralizes; h is the thickness of the enamel layer. Small circles represent schematic SIMS sample spots. Modified from Zazzo et al. (2012).

where δ_{ei} is the isotope value of fully mineralized enamel at position i, oriented parallel to the appositional surface, and δ_{mi} is the initial isotope value. This is summed with the average isotope values of the input signal over length l_m weighted according to the remaining mineralization. Additional time-averaging occurs when sampling through the thickness of enamel (h), which integrates enamel from multiple appositional layers. A column of enamel (i_c), whose thickness corresponds with volume i, drilled perpendicular to the growth axis through its entire thickness, can be modeled as:

$$\delta_{ci} = \frac{1}{l_a} \sum_{n=i-l_a}^{i} \delta_{e_n} \tag{2}$$

where δ_{ci} is the isotope value for each column. Finally, attenuation due to varying sample pit length (l_s) that does not extend through the entire thickness of enamel can be modeled by the following:

$$\delta_{di} = \frac{1}{l_s} \sum_{n=i-\frac{1}{2}l_s}^{i-1+\frac{1}{2}l_s} \delta_{c_n} \tag{3}$$

This forward model was originally developed for continuously-growing teeth, such as hippopotamus canines or rodent incisors, but it has been used to describe time-averaging in teeth with definite growth as well (Zazzo et al., 2005, 2010, 2012). However, measurements of both continuously and non-continuously growing teeth with known inputs show some deviations from the model, suggesting that assumptions of linear tooth growth and mineralization may represent an oversimplification (Podlesak et al., 2008; Zazzo et al., 2010, 2012). A mathematical inverse model has also been developed, which can be used to reconstruct input signals from attenuated intra-tooth isotope profiles (Passey et al., 2005). While tooth growth rates can be estimated in fossil animals using histological analysis of incremental features and intra-tooth isotope measurements, it is not possible to directly measure mineralization patterns in fossil tooth germs due to diagenetic re-mineralization of immature enamel (Tafforeau et al., 2007; Metcalfe and Longstaffe, 2012). Therefore, inverse models are difficult to extend to fossil taxa whose maturation parameters are not fully known.

Modifying the sampling strategy can reduce signal attenuation in measured intra-tooth profiles. Decreasing surface enamel sample spot size beyond the capacity of conventional drilling (typically several mm^3 of enamel) is not expected to improve signal resolution, as individual intra-tooth samples always represent isotope input blurred over the period of enamel maturation regardless of sample volume (Passey and Cerling, 2002; Balasse, 2003). Modifying the direction and placement of sampling to account for the spatial pattern of enamel growth represents a more effective strategy. To account for the geometry of matrix deposition, sampling can follow the incremental growth features on the enamel surface or in cross section, oblique to the growth axis (i.e. parallel to the forming front of matrix deposition). While this may reduce attenuation from sampling by preventing integration across different appositional growth layers, attenuation from amelogenesis is unaltered (Passey and Cerling, 2002; Zazzo et al., 2005). Sampling strategies that account for the geometry of mineralization, and target specific enamel regions characterized by high initial mineralization or more rapid maturation, represent a more promising approach (Passey and Cerling, 2002; Balasse, 2003; Zazzo et al., 2005, 2012; Tafforeau et al., 2007).

The innermost layer is a zone of aprismatic enamel extending <20 μm from the enamel–dentine junction (EDJ) (Allan, 1967; Suga, 1979, 1982, 1983, 1989; Tafforeau et al., 2007). Previous studies suggest that the innermost layer is more highly mineralized than other enamel layers when the maturation stage begins (Allan, 1959; Glick, 1979; Suga, 1979, 1982, 1983, 1989; Tafforeau et al., 2007); therefore, the innermost layer may retain an isotope signal that is less attenuated than in other layers and more closely follows the chronology of incremental features. Inner enamel can be sampled by microdrilling, and applications of this approach on steers fed an experimentally controlled diet (Zazzo et al., 2005) and a fossil Columbian mammoth (Metcalfe and Longstaffe, 2012) succeeded in recovering less attenuated intra-tooth isotope time-series. However, the effective spatial resolution of existing stable isotope microsampling methods, including micromilling (ca. 25–100 μm) (Zazzo et al., 2005) as well as laser ablation (ca. 100–200 μm) (Passey and Cerling, 2006) or earlier SIMS analysis (ca. 25 μm) (Aubert et al., 2012), is insufficient to discretely sample the innermost layer. Recent developments in secondary ion mass spectrometry (SIMS) allow *in situ* $\delta^{18}O$ measurements with approximately 4–5 μm beam spot size and an analytical precision of typically <1.0‰ (spot-to-spot) (Kita et al., 2009, 2011). These spots are small enough to allow *in situ* $\delta^{18}O$ measurements within the innermost enamel layer and reduce or prevent mixing

with adjacent layers. As with the *in situ* laser ablation technique, SIMS cannot discriminate between the oxygen in PO_4 (91.5%), CO_3 (5.6%), and OH^- (2.9%) of tooth enamel bioapatite (Passey and Cerling, 2006; Aubert et al., 2012). Therefore, *in situ* $\delta^{18}O$ analysis of tooth enamel with SIMS should reflect bulk-mineral composition.

The aims of this study are to estimate the pattern of mineralization within the innermost layer of mammalian tooth enamel, validate the use of SIMS for *in situ* $\delta^{18}O$ analysis of tooth enamel, and evaluate the potential of *in situ* $\delta^{18}O$ measurements by SIMS within the innermost enamel layer. We use SIMS to analyze incisor enamel from a woodrat (*Neotoma cinera*) (Fig. 2) included in a water-switch experiment (Podlesak et al., 2008). Rodent incisors have been used widely in studies of enamel development because they are continuously growing, and therefore contain all stages of enamel formation within individual specimens (Allan, 1967; Hiller et al., 1975; Glick, 1979; Suga, 1979; Smith, 1998). Rodent teeth form rapidly compared to other mammals, and a growth rate of 0.7 mm/day was estimated indirectly for this specimen based on best fit between predicted and observed data using the forward model described above (Podlesak et al., 2008). A number of techniques are available for assessing the geometry and rate of enamel mineralization, including microradiography (Hoppe et al., 2004), conventional and synchrotron X-ray microtomography (μCT) (Wong et al., 2000; Tafforeau et al., 2007), phosphorus concentration (Hiller et al., 1975; Lundgren et al., 1998; Passey and Cerling, 2002), and backscattered electron imaging in the scanning electron microscope (BSE-SEM) (Boyde and Jones, 1983; Gomez and Boyde, 1994; Bloebaum et al., 1997). We use BSE-SEM imaging, which provides sufficient image resolution to identify innermost enamel, to examine the pattern of enamel maturation throughout the enamel layer in the woodrat incisor as well as developing teeth from two wild ungulates, including a horse (*Equus ferus przewalskii*) molar from Mongolia and a hippopotamus (*Hippopotamus amphibius*) canine from Arabuko-Sokoke National Park, Kenya. In a previously reported study including the woodrat individual, a shift of 16.0‰ for $\delta^{18}O$ was measured during the water-switch in the breath CO_2, a proxy for body water that represents the input signal for enamel oxygen (Podlesak et al., 2008). We combine this natural label with measurements of enamel mineralization to test predictions of the forward model and to evaluate alternative sampling strategies with a comparison between intra-tooth SIMS $\delta^{18}O$ profiles from discrete enamel layers within the right incisor and an intra-tooth $\delta^{18}O$ profile from the enamel surface generated previously by laser ablation of the left incisor (Podlesak et al., 2008).

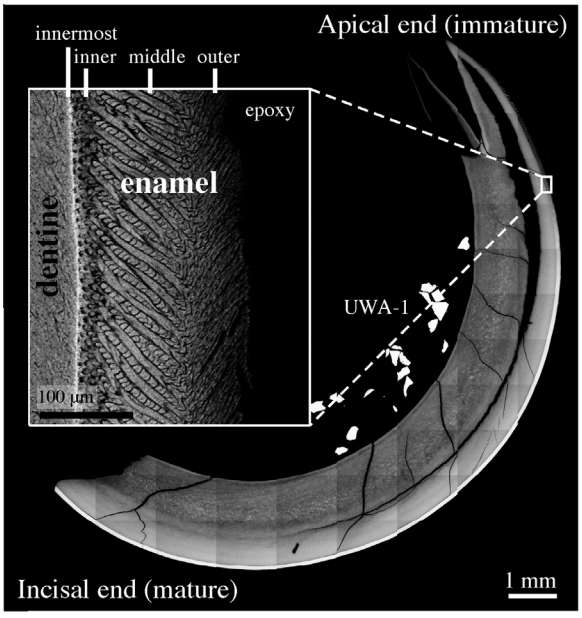

Fig. 2. BSE-SEM image of woodrat incisor. Inset: immature enamel. The innermost enamel layer is visible as the whiter line adjacent to dentine.

2. MATERIALS AND METHODS

2.1. Sample preparation and imaging

The right woodrat maxillary incisor was derived from a previously described water-switch experiment using ^{18}O-labeled water (individual #21 in Podlesak et al., 2008). The animal was housed at the University of Utah's animal facilities after being trapped in Summit County, Utah. The animal's water source was switched from 15.0 ± 0.2‰ to -16.1 ± 0.2‰ while diet food was held constant. The switch occurred after 127 days of drinking the enriched drinking water. The animal was sacrificed 27 days after drinking depleted water, and the incisors were subsequently extracted. Breath samples were collected during the experiment for isotope analysis of $\delta^{18}O$ in CO_2 by injecting the sample into a gas chromatography column attached to a Finnigan MAT 252 mass spectrometer. Values of $\delta^{18}O$ of mature enamel from the left incisor have been previously analyzed using a CO_2 laser and conventional H_3PO_4 methods. Additional details of these procedures are available elsewhere (Podlesak et al., 2008).

The right upper woodrat incisor was embedded in the center of a 25 mm round epoxy-mount along with grains of UWA-1 fluorapatite standard (Fig. 2). To minimize instrumental bias associated with sample position the tooth and standard grains were placed within 5 mm of the center of the mount (Kita et al., 2009). After polishing, surface topography was assessed at a submicron scale with a PhaseView® optical profilometer (Palaiseau, France). Due to the presence of large cracks (>200 μm), additional epoxy impregnation and polishing were required. This was necessary because sample topography deforms ion trajectories and significantly impacts the precision and accuracy of oxygen isotope measurements with SIMS and must be reduced to a few μm (Kita et al., 2009). After final polishing and gold coating, the surface topography was again assessed at a submicron scale with a Zygo optical profilometer (Middlefield, Connecticut). After ion microprobe analysis, sample spots were examined using a FEI Nova NanoSEM® (Hillsboro, Oregon) at 4 kV 0.23 nA, and a 5.1–5.2 mm working distance.

For analysis of tooth growth and mineralization, specimens were imaged embedded in epoxy and uncoated in variable pressure mode (50 Pa) using a Zeiss EVO-50® (Thornwood, New York) scanning electron microscope in BSE-SEM imaging mode at 15 kV, 600 pA, and 8.5-mm working distance. The woodrat specimen was imaged with the fluorapatite standard, while the ungulate specimens were imaged with two standards, including 99% pure aluminum (Al) with a mineral density similar to mature enamel and an iodinated methacrylate standard ($C_{22}H_{25}O_{10}I$) with a mineral density between dentine and enamel (Boyde et al., 1995; Howell et al., 1998). Image montages were acquired automatically using Zeiss SmartStich® software. ImageJ (NIH) was used to measure enamel thickness in immature enamel. The length of apposition l_a is defined as the length over which enamel reaches its maximum thickness, which corresponds to the interval of matrix deposition. The intensity (gray level) of individual pixels of BSE-SEM images of hard tissues is related to the number of measured backscattered electrons, which is proportional to the mean atomic number of the material and to weight percent mineral (Bloebaum et al., 1997).

ImageJ was used to measure gray levels of enamel transects parallel to the axis of growth through the innermost, inner, middle, and outer enamel layers (Fig. 2). Gray levels range from 0 for black (no mineral) and 255 for white (most mineral), and these transects were used to assess the pattern of mineralization after the completion of matrix deposition. The maturation length l_m is defined as the length over which the outer enamel layer, the last to fully mature, reaches final mineralization. Gray levels were also measured of mature enamel and mature dentine at the incisal, or coronal, end of the tooth to determine mineralization levels of each dental tissue at full maturity. For the woodrat specimen, the fluorapatite standard was used to estimate proportional mineralization from gray level measurements, with a gray level of 252 corresponding with 100% mineral and a gray level of 0 (epoxy) representing 0% mineral. The breath CO_2 input signal and these maturation parameters were used to predict intra-tooth enamel $\delta^{18}O$ values within discrete maturation layers with the forward model. For ungulate specimens, the Al standard was used to estimate mineralization from gray levels. Gray levels of 222 and 252 correspond with 99% mineral in the horse and hippopotamus image, respectively, and gray level of 0 (epoxy) represents 0% mineral.

The width of the innermost enamel layer was determined by measuring the width of the zone of high gray values at regular intervals (woodrat, 100 μm; horse, 500 μm; hippopotamus, 1000 μm) over the length of maturation. The identification of non-innermost enamel layers follows previous descriptions of rodent and ungulate tooth enamel. Rodent incisor enamel is divided into two primary groups, containing decussating enamel (*Portio Interna*, PI) and radial enamel (*Portio Externa*, PE) (Boyde, 1978; Martin, 1997). Decussating enamel in Myomorph incisors is identified as the portion of enamel with alternating one-prism-thick (uniserial) zones, which relate to periodic variation in prism orientation and have a sigmoid curvature (Boyde, 1978; Hilson, 2005). These are called Hunter-Schreger Bands when appearing as an optical phenomenon in polarizing microscopy of thin sections. Therefore, for the woodrat specimen the inner layer corresponds to the inner portion of the PI with bands angled approximately 45° relative to the EDJ and which in immature enamel can appear as oval prisms embedded in inter-prismatic enamel (Fig. 2). The middle layer corresponds with the outer portion of the PI with bands angled approximately 90° from the EDJ. The outer layer corresponds with the PE, which lacks decussating enamel. These layers have previously been characterized as following distinct maturation patterns (Suga, 1979). In the ungulate specimens, the outer layer corresponds to a previously described zone adjacent to the enamel surface that mineralizes slowly, and is less mineralized than the middle layer until the end of maturation (Suga, 1983). The width of the outer layer was determined by measuring the width of this zone of low gray values at regular intervals (horse, 500 μm; hippopotamus, 1000 μm) over the length of maturation. The inner and middle layers correspond to equal portions of the remaining enamel between the innermost and outer layers.

2.2. Secondary ion mass spectrometry (SIMS)

Oxygen isotope analyses were performed with a Ametek Cameca IMS-1280 (Paris, France) high resolution, multi-collector ion microprobe at the WiscSIMS lab, University of Wisconsin–Madison using a $^{133}Cs^+$ primary ion beam with an intensity of 35–40 pA, focused to approximately 4–5-μm beam-spot size (Kita et al., 2009, 2011; Valley and Kita, 2009). Sample spots were placed within mature enamel along the axis of growth moving from the incisal (older) to apical (newer) enamel within the innermost, inner, and middle/outer enamel layers (Fig. 3). The innermost layer was identified visually during the analytical session as a thin, aprismatic layer adjacent to the EDJ. Analytical conditions were comparable to those previously reported for work at WiscSIMS (Kozdon et al., 2009). The secondary O^- ions were detected simultaneously by a Faraday cup ($^{16}O^-$) and an electron multiplier ($^{18}O^-$). The count

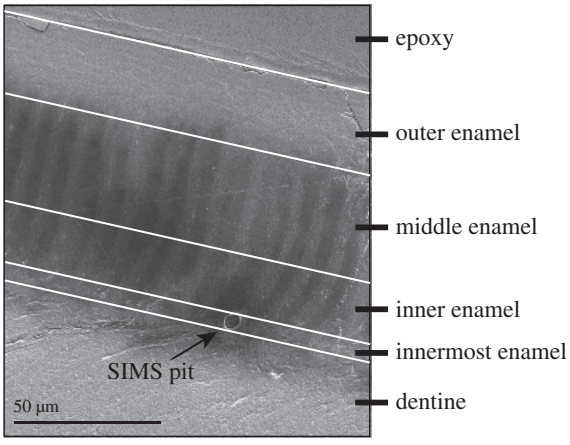

Fig. 3. SEM image of enamel, with sample spot within the innermost enamel layer. Enamel decussation, which relates to variation in prism orientation, is visible as alternating dark and light bands.

rates for $^{16}O^-$ were 3.5 to 4.2 × 10^7 cps. The total analytical time per spot was about 7 min including pre-sputtering (2 min), automatic centering of the secondary ion image in the field aperture (ca. 2 min) and analysis (ca. 3 min). Grains of UWA-1 were mounted with random orientations in the center of the sample and were measured in at least four spots before and after every 9–12 sample analyses. The resulting average value bracketing the samples was used for instrumental drift correction. Reproducibility of the individual spot analyses of UWA-1 standard (bracketing samples) is assigned as analytical precision of unknown samples, with a mean of 0.80‰ varying from 0.56‰ to 1.3‰ (±2 SD). After analysis at WiscSIMS, analysis pits were examined with SEM to ensure each pit does not overlap with dentine, surface discontinuities, or epoxy resin, as the isotope measurements from such pits would be considered compromised. The distance from the EDJ to the nearest edge of *in situ* SIMS analysis pits was measured to assign each pit to innermost, inner, middle/outer enamel layers. The residual sum of squares, or sum of squared errors of prediction (SSE), is used to calculate discrepancy between measured isotope data and forward model predictions.

3. RESULTS

3.1. Tooth growth and mineralization

3.1.1. Woodrat

Enamel thickness h increases to a maximum of 110 μm over 2.8 mm, which corresponds to the length of apposition l_a (Fig. 4). Given a growth rate of 0.7 mm/day, the rate of growth in thickness can be estimated as 39 μm/day. Therefore, at a given point along the length of the tooth, enamel at the surface represents matrix deposited 4 days later than enamel along the EDJ. Enamel thickness increases in a nonlinear pattern with alternating rapid and slow growth over mean intervals of 0.2 and 0.5 mm, respectively (Fig. 4). At the beginning of maturation, at maximum width, the width of the inner, middle, and outer layers is approximately 25, 55, and 24 μm, respectively. The width of the innermost enamel layer is 6 μm and does not decrease throughout maturation. Total enamel thickness decreases to approximately 90 μm in fully mature enamel (Fig. 4). The width of inner, middle, and outer layers in mature enamel is approximately 14, 50, and 20 μm, respectively.

Gray levels of the innermost enamel layer are high at the initiation of the maturation stage, quickly increasing beyond the level of mature dentine (Fig. 5). The other layers begin at low gray levels, but in the inner and middle layers gray levels increase rapidly and surpass mature dentine by approximately 2 mm along the maturation stage. Gray levels of the outer layer increase beyond mature dentine at approximately 2.5 mm, remain lower than other layers for the majority of maturation, and is the last layer to fully mature. The final gray level values for each layer were similar. The maturation length l_m for the entire layer of enamel is 5 mm, while the maturation length l_m of only the innermost layer is 2.8 mm (Fig. 5). The total time from initial matrix formation for enamel to reach full maturity is estimated at 11.1 days.

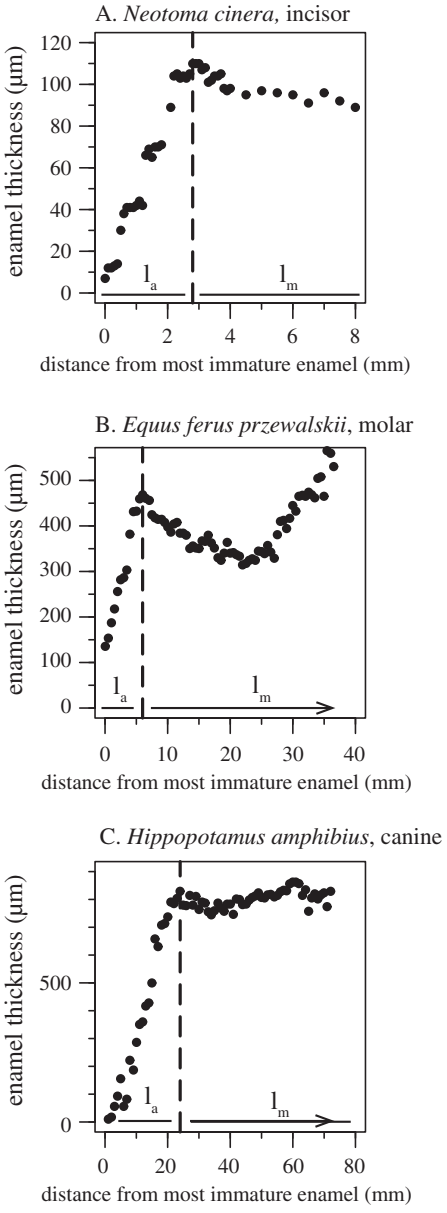

Fig. 4. Enamel thickness measurements from the beginning of matrix deposition through the maturation stage. (A) Enamel thickness measurements of the woodrat tooth. Measurements are in 100 μm increments from 1 to 4 mm and 500 μm increments from 4 to 8 mm. (B) Enamel thickness measurements of the horse tooth. Measurements are in 500 μm increments. Arrow indicates that maturation extends in length beyond the limits of the specimen (C) Enamel thickness measurements of the hippopotamus tooth. Measurements are in 1000 μm increments. Arrow indicates that maturation extends in length beyond the limits of the specimen.

Fully mineralized enamel has a mean gray level of 239 (on a scale of 0–255) and fully mineralized dentine has a mean gray level of 183. Comparison to the fluorapatite standard representing 100% mineral provides mineralization estimates of 95% and 73% for mature enamel and dentine, respectively (Fig. 5). These values provide a baseline for estimating mineralization from gray levels of immature

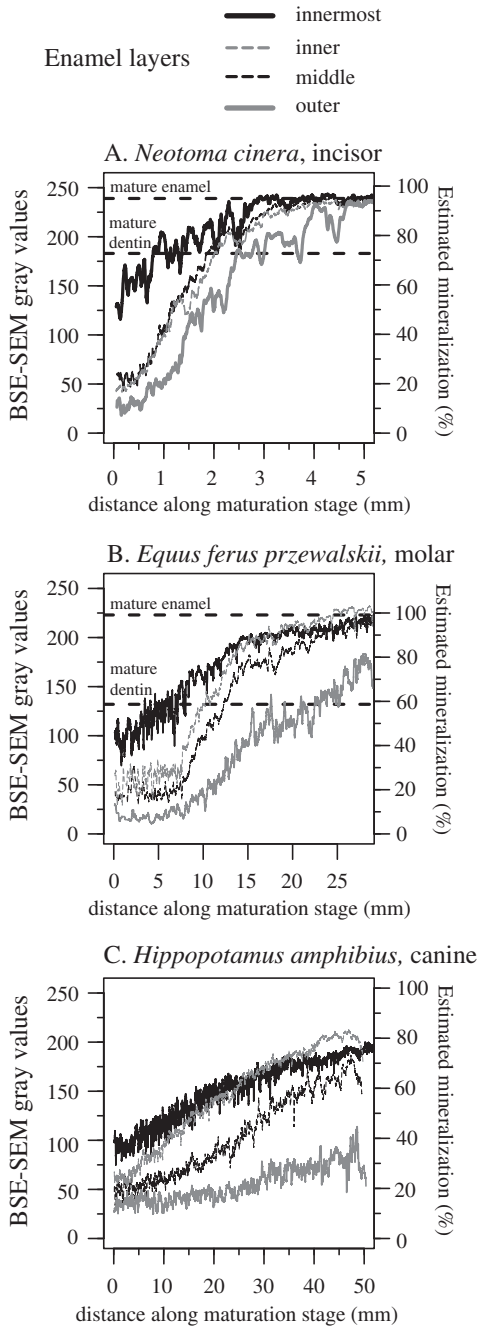

Fig. 5. BSE-SEM gray level transects through the length of maturation of the innermost, inner, middle, and outer enamel layers for the woodrat (A), horse (B), and hippopotamus (C). Gray levels are recorded every 1.5 μm in (A), and every 0.9793 μm in (B) and (C). Fifty-μm moving averages in (A) and 100-μm moving averages in (B) and (C) are used to smooth variability reflecting enamel immaturity as well as small cracks and other surface discontinuities introduced by repeated grinding and polishing procedures.

enamel. Mineralization for the innermost enamel layer begins at 48%, while the inner, middle, and outer layers begin at 17%, 19% and 11%, respectively (Fig. 5). The mineralization of all enamel except the innermost enamel layer weighted by width contribution is 17%. The forward model parameter f_i (initial mineral content) is proportional to fully mineralized enamel (95%), and is 51% for innermost enamel and 18% for non-innermost enamel.

3.1.2. Horse

Enamel thickness h increases to 469 μm over 6 mm, which corresponds to the length of apposition l_a. The width of the innermost and outer enamel layers is 12 and 14 μm, which does not change throughout maturation. At the beginning of maturation, the width of the inner and middle layers is 68 μm. The width of the inner and middle layers in mature enamel is 237 μm. Enamel thickness varies between 314 and 490 μm throughout the maturation stage (Fig. 4).

Gray levels of the innermost enamel layer are high early in the maturation stage, and quickly increase beyond the level of mature dentine (Fig. 5). The other layers begin at low gray levels and exhibit a delay between the onset of maturation and an increase in mineralization. The maturation length l_m of the innermost, inner, and middle layers is 28 mm. The mineralization of the outer layer increases more gradually, and does not reach final maturity within the length of enamel present in this specimen; therefore, the length of maturation for the entire layer of enamel cannot be estimated for this specimen.

Mature enamel, without the immature outer layer, has a mean gray level of 221 and mature dentine has a mean gray level of 132. Comparison to the Al standard representing 99% mineral provides mineralization estimates of 98% and 59% for mature enamel and dentine, respectively (Fig. 5). Mineralization for the innermost enamel layer begins at 46%, while the inner, middle, and outer layers begin at 26%, 19% and 13%, respectively (Fig. 5). The initial mineralization of all enamel except the innermost enamel layer weighted by width contribution is 22%. The initial mineral content f_i, proportional to mature enamel is 47%, 27%, 19% and 13% for the innermost, inner, middle, and outer layers, respectively. The initial mineral content f_i is 22% for all enamel except the innermost enamel layer, weighted by width contribution.

3.1.3. Hippopotamus

Enamel thickness h increases to a maximum of 828 μm over 24.0 mm, which corresponds to the length of apposition l_a. The width of the innermost and outer enamel layers is 15 and 14 μm, which does not change throughout maturation. At the beginning of maturation, the width of the inner and middle layers is 399.5 μm. Total enamel thickness remains relatively stable across the remaining length of the tooth fragment, varying between 744 and 862 μm (Fig. 4).

Gray levels of the innermost enamel layer are higher than other layers early in the maturation stage (Fig. 5). Gray levels of the inner layer increases beyond the innermost layer at approximately 25 mm, while gray levels from the middle and outer layers remain lower than both the innermost and inner layers. The mineralization of the outer layer increases slowly and remains <50% along the full length of this specimen. The full maturation stage is not represented, and no enamel layer reaches maturity; therefore, gray levels for mature enamel and dentine and the

length of maturation l_m cannot be estimated. Comparison to the Al standard representing 99% mineral provides mineralization estimates of 39% for the innermost enamel layer, and 27%, 19%, and 11% for inner, middle, and outer layers, respectively, at the beginning of the maturation stage.

3.2. Oxygen isotopes

For comparison with tooth enamel $\delta^{18}O$ values, breath CO_2 $\delta^{18}O$ values are converted to equivalent laser enamel values with known isotopic spacing first between breath and conventional H_3PO_4 enamel analysis $\varepsilon^*_{\text{enamel-breath}}$ and second between conventional and laser ablation enamel analysis $\varepsilon^*_{\text{laser-conv}}$. Time (h) of breath samples is converted to equivalent length (mm) using the previously reported enamel growth rate for this individual (Podlesak et al., 2008). While breath and laser $\delta^{18}O$ values are reported relative to VSMOW, the fluorapatite standard UWA-1 is not yet calibrated relative to this international standard. SIMS values require correction for instrumental mass fractionation based on a calibrated standard that is similar in mineralogy and composition. The raw SIMS values have been adjusted by adding 2.7‰ to each analysis, which brings the SIMS $\delta^{18}O$ values into approximate agreement with laser ablation analyses in the pre-switch region of the tooth (<0.1 cm for SIMS and <0.3 cm for laser). This is a reasonable value for instrumental bias of oxygen isotope ratios measured with the procedures of this study (Valley and Kita, 2009). The intra-tooth $\delta^{18}O$ profile within the innermost enamel layer represents analysis pits at distances of 0.4–2.8 μm (mean = 1.9) from the EDJ, where all or a majority of enamel within each spot was derived from the innermost enamel layer (Fig. 6). The inner enamel profile represents analysis pits 3.1–9.6 μm (mean = 4.3) from the EDJ, where all or a majority of enamel within each spot was derived from outside the innermost layer. The middle/outer enamel layer profile represents analysis pits 58–76 μm (mean = 66) from the EDJ, clustered near the boundary between these layers. Laser ablation $\delta^{18}O$ values were obtained by sampling the enamel surface with pits that extend partially through the enamel layer, and represents the middle/outer enamel layers.

The enamel of contralateral rodent incisors reach full mineralization at different lengths from the apex (Wong et al., 2000); therefore, the locations of *in situ* $\delta^{18}O$ SIMS analyses on the right incisor must be adjusted for comparison with *in situ* $\delta^{18}O$ laser ablation analyses on the left incisor. Additionally, because enamel near the surface is deposited later than enamel near the EDJ, an additional adjustment is needed to compare $\delta^{18}O$ profiles from different enamel layers. The alignment between laser and breath CO_2 $\delta^{18}O$ values is unchanged from previously reported values (Podlesak et al., 2008). To account for differences in growth between the left and right incisors, SIMS $\delta^{18}O$ values analyses were aligned with laser $\delta^{18}O$ values by adding 0.11 cm to the distance from incisal end of all SIMS values, which represents the difference in distance from incisial tip to immature enamel. The middle/outer SIMS profile is within the same appositional layers as integrated by laser spots, but inner and innermost SIMS profiles were shifted by an additional 0.14 mm (50% of apposition length) to account for their position near the EDJ. *In situ* SIMS $\delta^{18}O$ values are summarized in Fig. 7, and reported in Fig. A.1 and Table A.1 in the Appendix.

The innermost enamel forward model reflects the distinct maturation parameters in that layer, while the inner and middle/outer forward models are the same since the maturation parameters outside the innermost layer are similar. The forward model used to predict SIMS intra-tooth profiles is computed using Eq. (1) and accounts only for attenuation during amelogenesis, as analysis pits are small enough to negate significant integration of multiple appositional layers. As previously reported, the forward model used to predict the laser ablation intra-tooth profile is computed using Eqs. (1), (2), and (3) and reflects attenuation during amelogenesis as well as sampling, as laser pits extend partially through the enamel layer and integrate multiple apposition layers (Podlesak et al., 2008). *In situ* $\delta^{18}O$ profiles of the innermost, inner, and middle/outer enamel layers were generated with SIMS. The middle/outer profile extends over a shorter length of enamel than the other profiles, and may have included a greater range in $\delta^{18}O$ values if extended over greater length. Despite this discrepancy, due to limited analytical time, there is a minor increase in

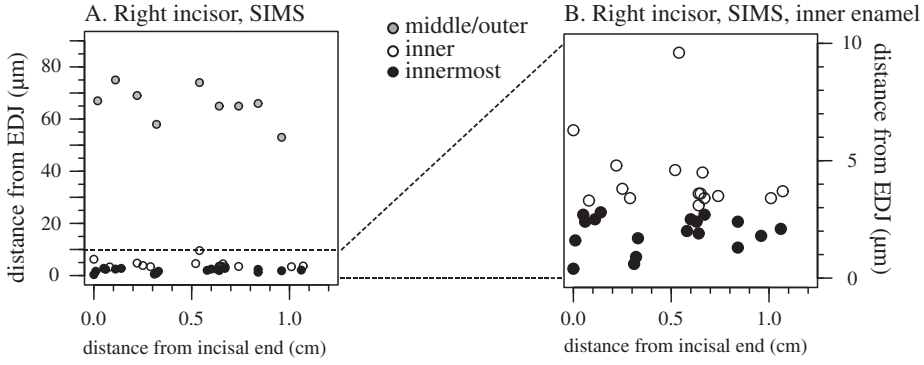

Fig. 6. (A) Distance measurements from the enamel-dentine junction (EDJ) to the nearest edge of *in situ* SIMS analysis pits within the innermost (closed circles), inner (open circles) and middle/outer (gray circles) enamel layers. (B) Measurements within only the inner (open circles) and innermost layers (closed circles).

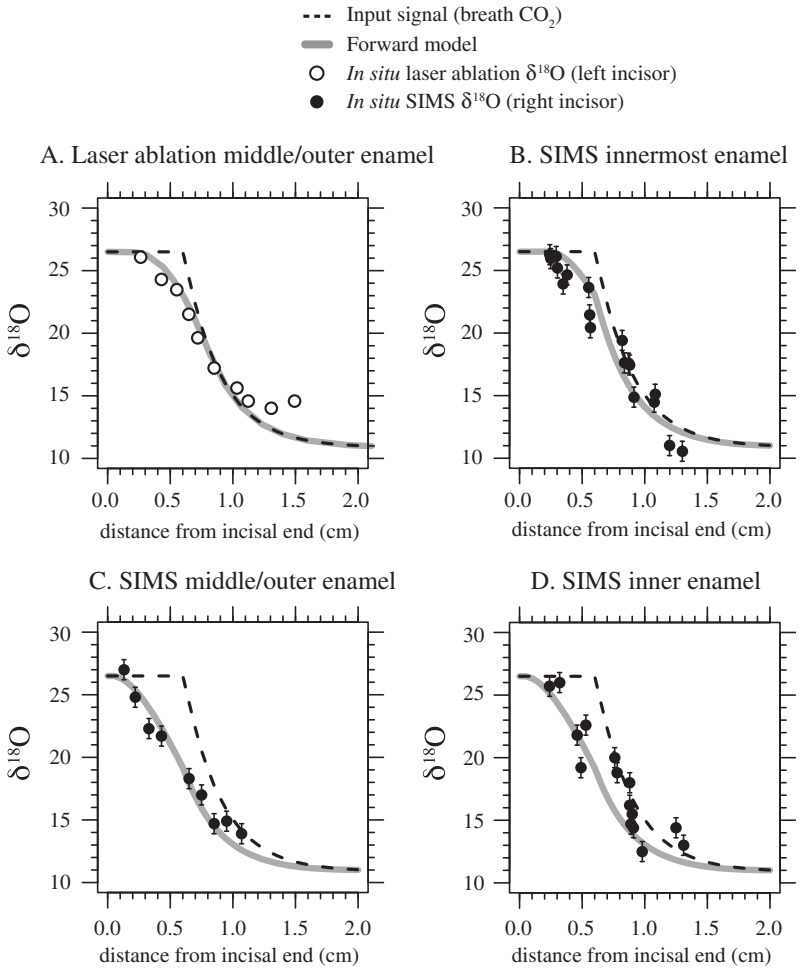

Fig. 7. Laser ablation (open circles) and SIMS (closed circles, ±2SD) *in situ* $\delta^{18}O$ values. Incisal end is opposite the root and represents the most mature enamel, with tooth growth to the right. For SIMS profiles, distances from incisal end that are displayed on the *X*-axis are corrected values, as explained in Section 3.2. Forward model using maturation parameters associated with either innermost or non-innermost enamel (gray line), and breath CO_2 input signal (dashed line). (A) middle/outer enamel; (B) innermost enamel; (C) middle/outer enamel; (D) inner enamel. SIMS data resemble forward model predictions, and the innermost layer records the most negative $\delta^{18}O$ values between 1.0 and 1.5 cm.

the range in $\delta^{18}O$ values at precision ±0.8‰ (2SD) from the middle/outer enamel (13.1‰) and inner enamel (13.5‰) intra-tooth profiles generated with SIMS compared to laser ablation of middle/outer enamel (12.1‰). However, only in the innermost enamel profile (15.7‰) does the range in $\delta^{18}O$ values match breath CO_2 (16.0‰).

The forward model used to predict the laser ablation intra-tooth middle/outer enamel profile provides a better fit (SSE = 18.4) than the model used to predict middle/outer enamel SIMS profile (SSE = 26.4). The forward model used to predict the innermost enamel profile generated with SIMS, using innermost enamel maturation parameters, provides a better fit (SSE = 46.9) than the model using non-innermost enamel maturation parameters (SSE = 86.7). The forward model used to predict the middle/outer enamel profile generated with SIMS, using non-innermost enamel maturation parameters, provides a better fit (SSE = 8.3) than the model using innermost enamel maturation parameters. The forward model using innermost enamel maturation parameters provides a better fit (SSE = 63.7) to the inner enamel profile generated with SIMS than the forward model using non-innermost maturation parameters (SSE = 76.4).

4. DISCUSSION

4.1. *In situ* oxygen isotope microsampling of enamel

Our results demonstrate that *in situ* SIMS analysis can be used for stable isotope microsampling of mammalian enamel with sample spots <10 μm. We used this technique to generate high-resolution intra-tooth $\delta^{18}O$ profiles within discrete layers of rodent incisor enamel, which record the $\delta^{18}O$ shift associated with the water switch and closely resemble forward model predictions (Fig. 7). *In situ* $\delta^{18}O$ values sampled with SIMS and laser ablation within middle/outer enamel reflect more gradual equilibration with switched water values, as predicted by the forward model. *In situ* $\delta^{18}O$ values sampled with SIMS within the inner enamel layer more closely reflect the forward model using

innermost, rather than non-innermost, enamel maturation parameters. This may reflect the more gradual mineralization of the outer layer (Fig. 5), which is incorporated in the estimation of non-innermost enamel maturation parameters. Isotope profiles obtained from the inner and middle/outer enamel layers with SIMS are moderately less attenuated in amplitude than laser ablation, reflected as an increase in range, but still fail to approach the predicted signal amplitude of breath CO_2 within the sampled interval of enamel. These discrepancies between predicted and measured $\delta^{18}O$ values suggest that the forward model may inaccurately estimate the rate and magnitude of isotopic change, which is consistent with previous observations in a comparison between breath CO_2 and laser ablation incisor enamel profiles from 5 additional woodrat individuals subjected to the same experimentally induced water-switch (Podlesak et al., 2008). The predicted and measured innermost enamel $\delta^{18}O$ values closely follow the input signal and matches the full amplitude of breath CO_2. This suggests that less attenuated isotope time-series can be recovered from the innermost enamel layer, and is consistent with the expectation that increased initial mineralization of this layer reduces signal attenuation from maturation (Zazzo et al., 2005; Tafforeau et al., 2007). Our observations also demonstrate that decreasing sample spot size beyond conventional sampling, when sampling outside the innermost enamel layer, may effectively remove attenuation from sampling but minimally reduce overall signal time-average due to amelogenesis.

The similarity between *in situ* laser ablation and SIMS $\delta^{18}O$ values from the pre-switch region of enamel suggests that SIMS represents bulk mineral composition. The $\delta^{18}O$ offset of 2.7‰ between SIMS (depleted) and laser ablation (enriched) is consistent with incomplete mixing of oxygen-bearing phases of tooth enamel during *in situ* laser ablation and a bias towards oxygen in CO_3, which is the ^{18}O-enriched phase (Passey and Cerling, 2006). Additionally, while variation in crystal orientation may decrease precision of *in situ* SIMS $\delta^{18}O$ analyses of some oxides (Kita et al., 2011), our analyses of multiple grains of UWA-1 fluorapatite standard that are mounted with random orientations demonstrates no measurable effect at precision of ±0.8‰ (2SD). Finally, uncorrected *in situ* SIMS $\delta^{18}O$ values are shifted toward the incisal end compared to *in situ* laser ablation analyses, due to differences in sample integration of enamel layers and differences in tooth growth between the left and right incisors (Fig. A.1). Future application of *in situ* SIMS analysis to tooth enamel will require similar corrections when making comparisons between intra-tooth profiles recovered with different sampling techniques or from different teeth from an individual.

4.2. ENAMEL GROWTH AND MINERALIZATION

Our BSE-SEM results demonstrate the effectiveness of this technique for estimating maturation parameters of mammalian tooth enamel needed to guide stable isotope microsampling. The narrow (<20 μm) innermost layer with high initial mineralization can be identified in teeth that are both continuously growing (woodrat incisor and hippopotamus canine) and non-continuously growing (horse molar). In the woodrat, mineral content estimates of mature enamel and dentine match expected values, and previously reported lengths of apposition and maturation estimated with μCT data from the contralateral incisor are in close agreement with those presented here (Podlesak et al., 2008). Our measured maximum width of the enamel layer, and the slight decline in thickness in fully mature enamel, agrees with previous measurements of developing rodent incisor enamel (Glick, 1979; Podlesak et al., 2008), as does the multi-stage, spatially diffuse process of enamel mineralization with previous microradiogram (Suga, 1979), μCT (Wong et al., 2000), and BSE-SEM (Gomez and Boyde, 1994) analyses of rodent incisors. Additionally, our description of high initial mineralization within the innermost layer accords with previous microradiogram analyses of developing rodent incisor enamel (Suga, 1979).

Our analyses of developing horse and hippopotamus teeth support previously reported details of ungulate tooth enamel formation (Suga, 1982, 1983; Tafforeau et al., 2007). Maturation occurs over a substantial length of tooth, and therefore time, and is not synchronous across the entire layer of enamel. Our estimate for the total mineralization interval (the combined length of apposition l_a and maturation l_m) of 34 mm in the horse tooth agrees with previous estimates of 30–40 mm for horse cheek teeth, and corresponds to a period of ~1 year given vertical tooth growth estimates of 30–40 mm/year Sharp and Cerling, 1998; Hoppe et al., 2004). The mineralization interval in this hippopotamus canine has been previously estimated at 80 mm (Passey and Cerling, 2002), which corresponds to a period of approximately 2–6 years given growth rate estimates of 13–39 mm/year (Passey et al., 2005; Souron et al., 2012). Therefore, enamel maturation is not instantaneous and results in time-averaging of isotope profiles in teeth where individual intra-tooth samples from large mammalian herbivores integrate several months of input (Passey and Cerling, 2002; Balasse, 2003; Hoppe et al., 2004; Zazzo et al., 2005).

4.3. IMPLICATIONS FOR ENAMEL MODELING AND MICROSAMPLING

Assessing enamel maturation parameters in other animals is necessary to improve sampling protocols and the application of forward and inverse models to a wider range of taxa. The forward model can be improved by incorporating non-linear appositional growth and mineralization, particularly for non-continuously growing teeth (Zazzo et al., 2005, 2010, 2012). The presence of this narrow layer (<20 μm) has now been documented in ungulates (bovids, equids, rhinocerids, hippopotamids), canids, rodents, and primates (Suga et al., 1970, 1977; Suga, 1979, 1982, 1983, 1989; Tafforeau et al., 2007; this study), which suggests that *in situ* SIMS analysis of the innermost enamel layer can be applied to a wide range of mammalian taxa. *In situ* SIMS analysis also provides a means to empirically validate model predictions for discrete appositional or maturation layers

of the enamel, which cannot always be sampled using other techniques. Recovering less attenuated intra-tooth isotope variation from the innermost enamel layer will be particularly useful for validating the application of inverse models to extinct taxa, as diagenetic alteration of immature enamel precludes the direct estimation of maturation parameters in fossil tooth germs. However, because our experimentally controlled sample contained only a single, directional isotope switch we were unable to assess the effectiveness of sampling the innermost enamel layer for reducing attenuation of signal structure. Additionally, this approach cannot remove sources of signal attenuation that do not stem from enamel maturation or sampling, such as body fluid reservoir effects; therefore, no enamel sampling method can recover a truly unaltered environmental signal (Sharp and Cerling, 1998).

The rapid growth rate of rodent incisor enamel means that the intra-tooth profiles are subject to less extreme signal attenuation compared to large mammalian herbivores characterized by more slowly mineralizing enamel (Kohn, 2004). This is illustrated by the similarity between the laser ablation enamel profile and breath CO_2 in the woodrat. Therefore, the application of this technique to ungulates will provide greater gains in intra-tooth signal amplitude, relative to conventional sampling techniques. Spot-to-spot reproducibility of *in situ* SIMS analysis may preclude application to animals in some non-experimental settings, where isotopic variability is limited. However, studies of intra-tooth sampling on modern, archaeological, and/or fossil large mammalian herbivores demonstrate that isotopic variability of >3‰ in $\delta^{13}C$ and $\delta^{18}O$ can be recovered with conventional sampling techniques (Balasse 2003; Higgins and MacFadden, 2009; Balasse et al., 2005; Cerling et al., 2008; Fraser et al., 2008; Bernard et al., 2009; Hallin et al., 2012; Metcalfe and Longstaffe, 2012; Zhang et al., 2012). Additionally, it is possible to achieve spot-to-spot reproducibility of 0.3‰ with larger spots (10 to 15 μm) than those used here (Kita et al., 2009, 2011). This beam spot size may be used for sampling some larger mammals, where the innermost enamel layer extends 10–20 μm from the EDJ (Tafforeau et al., 2007; this study).

5. CONCLUSIONS

Our findings demonstrate that *in situ* analysis of tooth enamel with SIMS can resolve isotopic variability on a fine spatial scale. We successfully identify large variation in $\delta^{18}O$ values within a single tooth that correlates well to measured breath CO_2, and corresponds to the water-switch experienced by this individual. This technique is especially powerful for sampling the innermost enamel layer, which is characterized by different maturation parameters in both continuously and non-continuously growing mammal teeth and can provide less time-averaged signals compared to conventional sampling. While micron-scale analysis spots can effectively remove signal attenuation introduced by sampling, time averaging from mineralization remains significant when sampling gradually mineralizing enamel outside the innermost layer. Rodent incisor enamel mineralizes rapidly compared to other mammals; therefore, signal amplitude is only moderately attenuated regardless of sampling strategy. Sampling the innermost enamel layer is expected to provide greater signal gains relative to conventional sampling when analyzing large mammalian herbivore teeth, which are characterized by more slowly mineralizing enamel. These teeth record environmental input over greater periods of time (months to years) and represent important proxies for reconstructing seasonal-scale dietary and environmental variation.

ACKNOWLEDGMENTS

We thank B.H. Passey for providing samples and data, Brian Hess and Quintin Sahratian for assistance with sample preparation, and Matt DeLong for assistance with imaging. We thank Paul Tafforeau, Fred J. Longstaffe, and an anonymous reviewer for providing suggestions and comments. This research was funded by the New York Consortium of Evolutionary Primatology NSF DGE 0333415, NSF BCS 0621542, and Sigma Xi G20110315157181. Research support was also provided by the 2010 Max Planck Research Award to TGB, endowed by the German Federal Ministry of Education and Research to the Max Planck Society and the Alexander von Humboldt Foundation in respect of the Hard Tissue Research Program in Human Paleobiomics. WiscSIMS is partly supported by NSF (EAR03-19230, EAR10-53466).

APPENDIX A. SUPPLEMENTARY DATA

Supplementary data associated with this article can be found, in the online version, at http://dx.doi.org/10.1016/j.gca.2013.09.032.

REFERENCES

Allan J. H. (1959) Investigations into the mineralization pattern of human dental enamel. *J. Dent. Res.* **38**, 1096–1107.

Allan J. H. (1967) Maturation of enamel. In *Structural and Chemical Organization of Teeth* (ed. A. Miles). Academic Press, New York, pp. 467–494.

Aubert M., Williams I. S., Boljkovac K. and Moffat I. (2012) In situ oxygen isotope micro-analysis of faunal material and human teeth using a SHRIMP II: a new tool for palaeo-ecology and archaeology. *J. Archaeol. Sci.* **39**, 3184–3194.

Ayliffe L. K., Chivas A. and Leakey M. G. (1994) The retention of primary oxygen isotope compositions of fossil elephant skeletal phopshate. *Geochim. Cosmochim. Acta* **58**, 5291–5298.

Balasse M. (2002) Reconstructing dietary and environmental history from enamel isotopic analysis: time resolution of intra-tooth sequential sampling. *Int. J. Osteoarchaeol.* **12**, 155–165.

Balasse M. (2003) Potential biases in sampling design and interpretation of intra-tooth isotope analysis. *Int. J. Osteoarchaeol.* **13**, 3–10.

Balasse M., Ambrose S. H., Smith A. B. and Price T. D. (2002) The seasonal mobility model for prehistoric herders in the south-western Cape of South Africa assessed by isotopic analysis of sheep tooth enamel. *J. Archaeol. Sci.* **29**, 917–932.

Balasse M., Smith A. B., Ambrose S. H. and Leigh S. (2003) Determining sheep birth seasonality by analysis of tooth enamel oxygen isotope ratios: the Late Stone Age site of Kasteelberg (South Africa). *J. Archaeol. Sci.* **30**, 205–215.

Balasse M., Tresset A. and Ambrose S. H. (2005) Stable isotope evidence ($\delta^{13}C$, $\delta^{18}O$) for winter feeding on seaweed by Neolithic sheep of Scotland. *J. Zool.* **270**, 170–176.

Balasse M., Obein G., Ughetto-Monfrin J. and Mainland I. (2011) Investigating seasonality and season of birth in past herds: a reference set of sheep enamel stable oxygen isotope ratios. *Archaeometry* **54**, 349–368.

Bernard A., Daux V., Lécuyer C. and Brugal J.-P. (2009) Pleistocene seasonal temperature variations recorded in the $\delta^{18}O$ of Bison priscus teeth. *Earth Planet. Sci. Lett.* **283**, 133–143.

Bloebaum R. D., Skedros J. G., Vajda E. G., Bachus K. N. and Constantz B. R. (1997) Determining mineral content variations in bone using backscattered electron imaging. *Quatern. Res.* **20**, 485–490.

Boyde A. (1978) Development of the structure of the enamel of the incisor teeth in the three classical subordinal groups of the Rodentia. In *Development, Function and Evolution of Teeth* (eds. P. M. Butler and K. A. Joysey). Academic Press, London, pp. 43–58.

Boyde A. and Jones S. J. (1983) Backscattered electron imaging of dental tissues. *Anat. Embryol.* **168**, 211–226.

Boyde A., Davy K. W. M. and Jones S. J. (1995) Standards for mineral quantification of human bone by analysis of backscattered electron images. *Scanning* **17**(5 Suppl.), V6–V7.

Britton K., Grimes V., Dau J. and Richards M. P. (2009) Reconstructing faunal migrations using intra-tooth sampling and strontium and oxygen isotope analyses: a case study of modern caribou (*Rangifer tarandus* granti). *J. Archaeol. Sci.* **36**, 1163–1172.

Brookman T. H. and Ambrose S. H. (2012) Seasonal variation in kangaroo tooth enamel oxygen and carbon isotopes in Australia. *Quatern. Res.* **78**, 256–265.

Bryant J. D. and Froelich P. N. (1995) A model of oxygen isotope fractionation in body water of large mammals. *Geochim. Cosmochim. Acta* **59**, 4523–4537.

Bryant J. D., Froelich P. N., Showers W. J. and Genna B. J. (1996a) Biologic and climatic signals in the oxygen isotopic composition of Eocene–Oligocene equid enamel phosphate. *Palaeogeogr. Palaeoclimatol. Palaeoecol.* **126**, 75–89.

Bryant J. D., Koch P. L., Froelich P. N., Showers W. J. and Genna B. J. (1996b) Oxygen isotope partitioning between phosphate and carbonate in mammalian apatite. *Geochim. Cosmochim. Acta* **60**, 5145–5148.

Cerling T. E. and Harris J. M. (1999) Carbon isotope fractionation between diet and bioapatite in ungulate mammals and implications for ecological and paleoecological studies. *Oecologia* **120**, 347–363.

Cerling T. E. and Sharp Z. (1996) Stable carbon and oxygen isotope analysis of fossil tooth enamel using laser ablation. *Palaeogeogr. Palaeoclimatol. Palaeoecol.* **126**, 173–186.

Cerling T. E., Harris J. M., Hart J. A., Kaleme P., Klingel H., Leakey M. G., Levin N. E., Lewison R. L. and Passey B. H. (2008) Stable isotope ecology of the common hippopotamus. *J. Zool.* **276**, 204–212.

Chritz K. L., Dyke G. J., Zazzo A., Lister A. M., Monaghan N. T. and Sigwart J. D. (2009) Palaeobiology of an extinct Ice Age mammal: stable isotope and cementum analysis of giant deer teeth. *Palaeogeogr. Palaeoclimatol. Palaeoecol.* **282**, 133–144.

Codron J., Codron D., Sponheimer M., Kirkman K., Duffy K. J., Raubenheimer E. J., Mélice J. L., Grant R., Clauss M. and Lee-Thorp J. A. (2012) Stable isotope series from elephant ivory reveal lifetime histories of a true dietary generalist. *Proc. Biol. Sci.* **279**, 2433–2441.

DeNiro M. J. and Epstein S. (1978) Influence of diet on the distribution of carbon isotopes in animals. *Geochim. Cosmochim. Acta* **42**, 495–506.

Elliott J. C. (1997) Structure, crystal chemistry and density of enamel apatites. In *Dental Enamel (Ciba Foundation Symposium 205)* (eds. D. Chadwick and G. Cardew). Wiley Online Library, Chichester, UK, pp. 54–72.

Elliott J. C. (2002) Calcium phosphate biominerals. *Rev. Mineral. Geochem.* **48**, 427–453.

Elliott J. C., Holcomb D. W. and Young R. A. (1985) Infrared determination of the degree of substitution of hydroxyl by carbonate ions in human dental enamel. *Oecologia* **37**, 372–375.

Fisher D. C. and Fox D. L. (1998) Oxygen isotopes in mammoth teeth: sample design, mineralization patterns, and enamel–dentine comparisons. *J. Vert. Palaeontol.* **18**(3 Suppl.), 41A–42A.

Fox D. L. and Fisher D. C. (2001) Stable isotope ecology of a late Miocene population of Gomphotherium productus (Mammalia, Proboscidea) from Port of Entry Pit, Oklahoma, USA. *Palaios* **16**, 279.

Fox D. L. and Fisher D. C. (2004) Dietary reconstruction of Miocene Gomphotherium (Mammalia, Proboscidea) from the Great Plains region, USA, based on the carbon isotope composition of tusk and molar enamel. *Palaeogeogr. Palaeoclimatol. Palaeoecol.* **206**, 311–335.

Fraser R. A., Grün R., Privat K. and Gagan M. K. (2008) Stable-isotope microprofiling of wombat tooth enamel records seasonal changes in vegetation and environmental conditions in eastern Australia. *Palaeogeogr. Palaeoclimatol. Palaeoecol.* **269**, 66–77.

Frémondeau D., Cucchi T. and Casabianca F. (2012) Seasonality of birth and diet of pigs from stable isotope analyses of tooth enamel. *J. Archaeol. Sci.* **39**, 2023–2035.

Fricke H. C. and O'Neil J. R. (1996) Inter-and intra-tooth variation in the oxygen isotope composition of mammalian tooth enamel phosphate: implications for palaeoclimatological and palaeobiological research. *Palaeogeogr. Palaeoclimatol. Palaeoecol.* **126**, 91–100.

Fricke H. C., Clyde W. and O'Neil J. R. (1998) Intra-tooth variations in $\delta^{18}O$ (PO_4) of mammalian tooth enamel as a record of seasonal variations in continental climate variables. *Geochim. Cosmochim. Acta* **62**, 1839–1850.

Glick P. L. (1979) Patterns of enamel maturation. *J. Dent. Res.* **58**, 883–895.

Gomez S. and Boyde A. (1994) Correlated alkaline phosphatase histochemistry and quantitative backscattered electron imaging in the study of rat incisor ameloblasts and enamel mineralization. *Microsc. Res. Tech.* **29**, 29–36.

Hallin K. A., Schoeninger M. J. and Schwarcz H. P. (2012) Paleoclimate during Neandertal and anatomically modern human occupation at Amud and Qafzeh, Israel: the stable isotope data. *J. Hum. Evol.* **62**, 59–73.

Higgins P. and Macfadden B. J. (2009) Seasonal and geographic climate variabilities during the Last Glacial Maximum in North America: applying isotopic analysis and macrophysical climate models. *Palaeogeogr. Palaeoclimatol. Palaeoecol.* **283**, 15–27.

Hiller C. R., Robinson C. and Weatherell J. (1975) Variations in the composition of developing rat incisor enamel. *Calcif. Tissue Int.* **18**, 1–12.

Hilson S. (2005) *Teeth*. Cambridge University Press, New York.

Hoppe K., Stover S., Pascoe J. and Amundson R. (2004) Tooth enamel biomineralization in extant horses: implications for isotopic microsampling. *Palaeogeogr. Palaeoclimatol. Palaeoecol.* **206**, 355–365.

Howell P. G. T., Davy K. M. W. and Boyde A. (1998) Mean atomic number and backscattered electron coefficient calcula-

tions for some materials with low mean atomic number. *Scanning* **20**, 35–40.

Iacumin P., Bocherens H., Mariotti A. and Longinelli A. (1996) Oxygen isotope analyses of co-existing carbonate and phosphate in biogenic apatite: a way to monitor diagenetic alteration of bone phosphate? *Earth Planet. Sci. Lett.* **142**, 1–6.

Jones A. M., Iacumin P. and Young E. D. (1999) High-resolution $\delta^{18}O$ analysis of tooth enamel phosphate by isotope ratio monitoring gas chromatography mass spectrometry and ultraviolet laser fluorination. *Chem. Geol.* **153**, 241–248.

Julien M.-A., Bocherens H., Burke A., Drucker D. G., Patou-Mathis M., Krotova O. and Péan S. (2012) Were European steppe bison migratory? ^{18}O, ^{13}C and Sr intra-tooth isotopic variations applied to a palaeoethological reconstruction. *Quatern. Int.* **271**, 106–119.

Kirsanow K., Makarewicz C. and Tuross N. (2008) Stable oxygen ($\delta^{18}O$) and hydrogen (δD) isotopes in ovicaprid dentinal collagen record seasonal variation. *J. Archaeol. Sci.* **35**, 3159–3167.

Kita N. T., Ushikubo T., Fu B. and Valley J. W. (2009) High precision SIMS oxygen isotope analysis and the effect of sample topography. *Chem. Geol.* **264**, 43–57.

Kita N. T., Huberty J. M., Kozdon R., Beard B. L. and Valley J. W. (2011) High-precision SIMS oxygen, sulfur and iron stable isotope analyses of geological materials: accuracy, surface topography and crystal orientation. *Surf. Interface Anal.* **43**, 427–431.

Koch P. L., Fisher D. C. and Dettman D. (1989) Oxygen isotope variation in the tusks of extinct proboscideans: a measure of season of death and seasonality. *Geology* **17**, 515–519.

Koch P. L., Tuross N. and Fogel M. L. (1997) The effects of sample treatment and diagenesis on the isotopic integrity of carbonate in biogenic hydroxylapatite. *J. Archaeol. Sci.* **24**, 417–430.

Kohn M. J. (2004) Comment: tooth enamel mineralization in ungulates: implications for recovering a primary isotopic time-series, by B.H. Passey and T.E. Cerling (2002). *Geochim. Cosmochim. Acta* **68**, 403–405.

Kohn M. J., Schoeninger M. J. and Valley J. W. (1996) Herbivore tooth oxygen isotope compositions: effects of diet and physiology. *Geochim. Cosmochim. Acta* **60**, 3889–3896.

Kohn M. J., Schoeninger M. J. and Valley J. W. (1998) Variability in oxygen isotope compositions of herbivore teeth: reflections of seasonality or developmental physiology? *Chem. Geol.* **152**, 97–112.

Kohn M. J., Miselis J. L. and Fremd T. J. (2002) Oxygen isotope evidence for progressive uplift of the Cascade Range, Oregon. *Earth Planet. Sci. Lett.* **204**, 151–165.

Kozdon R., Ushikubo T., Kita N. T., Spicuzza M. and Valley J. W. (2009) Intratest oxygen isotope variability in the planktonic foraminifer *N. pachyderma*: real vs. apparent vital effects by ion microprobe. *Chem. Geol.* **258**, 327–337.

LeGeros R. Z., Trautz O. R., Klein E. and LeGeros J. P. (1969) Two types of carbonate substitution in the apatite structure. *Experientia* **25**, 5–7.

Longinelli A. (1984) Oxygen isotopes in mammal bone phosphate: a new tool for paleohydrological and paleoclimatological research? *Geochim. Cosmochim. Acta* **48**, 385–390.

Lundgren T., Persson L. G., Engström E. U., Chabala J., Levi-Setti R. and Norén J. G. (1998) A secondary ion mass spectroscopic study of the elemental composition pattern in rat incisor dental enamel during different stages of ameloblast differentiation. *Arch. Oral Biol.* **43**, 841–848.

Luz B., Kolodny Y. and Horowitz M. (1984) Fractionation of oxygen isotopes between mammalian bone-phosphate and environmental drinking water. *Geochim. Cosmochim. Acta* **48**, 1689–1693.

Martin T. (1997) Incisor enamel microstructure and systematics in rodents. In *Tooth Enamel Microstructure* (eds. W. von Koenigswald and P. M. Sander). Balkema, Rotterdam, Netherlands, pp. 163–175.

Metcalfe J. Z. and Longstaffe F. J. (2012) Mammoth tooth enamel growth rates inferred from stable isotope analysis and histology. *Quatern. Res.* **77**, 424–432.

Moss-Salentijn L., Moss M. and Yuan M. S.-T. (1997) The ontogeny of mammalian enamel. In *Tooth Enamel Microstructure* (ed. W. von Koenigswald). Balkema, Rotterdam, pp. 5–30.

Nelson S. (2005) Paleoseasonality inferred from equid teeth and intra-tooth isotopic variability. *Palaeogeogr. Palaeoclimatol. Palaeoecol.* **222**, 122–144.

Passey B. H. and Cerling T. E. (2002) Tooth enamel mineralization in ungulates: implications for recovering a primary isotopic time-series. *Geochim. Cosmochim. Acta* **66**, 3225–3234.

Passey B. H. and Cerling T. E. (2006) In situ stable isotope analysis ($\delta^{13}C$, $\delta^{18}O$) of very small teeth using laser ablation GC/IRMS. *Chem. Geol.* **235**, 238–249.

Passey B. H., Cerling T. E., Schuster G. and Robinson T. F. (2005) Inverse methods for estimating primary input signals from time-averaged isotope profiles. *Geochim. Cosmochim. Acta* **69**, 4101–4116.

Pellegrini M., Lee-Thorp J. A. and Donahue R. E. (2011) Exploring the variation of the $\delta^{18}O_p$ and $\delta^{18}O_c$ relationship in enamel increments. *Palaeogeogr. Palaeoclimatol. Palaeoecol.* **310**, 71–83.

Podlesak D. W., Torregrossa A., Ehleringer J. R., Dearing M. D., Passey B. H. and Cerling T. E. (2008) Turnover of oxygen and hydrogen isotopes in the body water, CO_2, hair, and enamel of a small mammal. *Geochim. Cosmochim. Acta* **72**, 19–35.

Robinson C., Kirkham J., Brookes S. J., Bonass W. A. and Shore R. C. (1995) The chemistry of enamel development. *Int. J. Dev. Biol.* **39**, 145–152.

Sakae T. and Hirai G. (1982) Calcification and crystallization in bovine enamel. *J. Dent. Res.* **61**, 57–59.

Sharp Z. and Cerling T. E. (1998) Fossil isotope records of seasonal climate and ecology: straight from the horse's mouth. *Geology* **26**, 219–222.

Shi J., Klocke A., Zhang M. and Bismayer U. (2005) Thermally-induced structural modification of dental enamel apatite decomposition and transformation of carbonate groups. *Eur. J. Mineral.* **17**, 769–775.

Smith C. E. (1998) Cellular and chemical events during enamel maturation. *Crit. Rev. Oral Biol. Med.* **9**, 128–161.

Souron A., Balasse M. and Boisserie J.-R. (2012) Intra-tooth isotopic profiles of canines from extant *Hippopotamus amphibius* and late Pliocene hippopotamids (Shungura formation, Ethiopia): insights into the seasonality of diet and climate. *Palaeogeogr. Palaeoclimatol. Palaeoecol.* **342–243**, 97–110.

Stevens R. E., Balasse M. and O'Connell T. C. (2011) Intra-tooth oxygen isotope variation in a known population of red deer: implications for past climate and seasonality reconstructions. *Palaeogeogr. Palaeoclimatol. Palaeoecol.* **301**, 64–74.

Suga S. (1979) Comparative histology of progressive mineralization pattern of developing incisor enamel of rodents. *J. Dent. Res.* **58**, 1025–1026.

Suga S. (1982) Progressive mineralization pattern of developing enamel during the maturation stage. *J. Dent. Res.* **61**, 1532–1542.

Suga S. (1983) Comparative histology of the progressive mineralization pattern of developing enamel. In *Mechanisms of Tooth Enamel Formation* (ed. S. Suga). Quintessence Publishing, Tokyo, pp. 167–203.

Suga S. (1989) Enamel hypomineralization viewed from the pattern of progressive mineralization of human and monkey developing enamel. *Adv. Dent. Res.* **3**, 188–198.

Suga S., Murayama Y. and Musashi T. (1970) A study of the mineralization process in the developing enamel of guinea pigs. *Arch. Oral Biol.* **15**, 597–608.

Suga S., Kamio N., Yoshida S. and Doh A. (1977) Progressive mineralization pattern of developing enamel of dog. *Jpn. J. Oral Biol.* **19**, 219–238.

Tafforeau P., Bentaleb I., Jaeger J. and Martin C. (2007) Nature of laminations and mineralization in rhinoceros enamel using histology and X-ray synchrotron microtomography: potential implications for palaeoenvironmental isotopic studies. *Palaeogeogr. Palaeoclimatol. Palaeoecol.* **246**, 206–227.

Valley J. W. and Kita N. T. (2009) In situ oxygen isotope geochemistry by ion microprobe. In *GAC/MAC Short Course: Secondary Ion Mass Spectrometry in the Earth and Planetary Sciences*, vol. 41 (ed. M. Fayek). Mineralogical Association of Canada, Toronto, Canada, pp. 19–63.

Wong F., Elliott J., Davis G. and Anderson P. (2000) X-ray microtomographic study of mineral distribution in enamel of mandibular rat incisors. *J. Anat.* **196**, 405–413.

Zazzo A., Lécuyer C. and Mariotti A. (2004) Experimentally-controlled carbon and oxygen isotope exchange between bioapatites and water under inorganic and microbially-mediated conditions. *Geochim. Cosmochim. Acta* **68**, 1–12.

Zazzo A., Balasse M. and Patterson W. P. (2005) High-resolution $\delta^{13}C$ intra-tooth profiles in bovine enamel: implications for mineralization pattern and isotopic attenuation. *Geochim. Cosmochim. Acta* **69**, 3631–3642.

Zazzo A., Balasse M. and Patterson W. P. (2006) The reconstruction of mammal individual history: refining high-resolution isotope record in bovine tooth dentine. *J. Archaeol. Sci.* **33**, 1177–1187.

Zazzo A., Balasse M., Passey B. H., Moloney A. P., Monahan F. J. and Schmidt O. (2010) The isotope record of short- and long-term dietary changes in sheep tooth enamel: implications for quantitative reconstruction of paleodiets. *Geochim. Cosmochim. Acta* **74**, 3571–3586.

Zazzo A., Bendrey R., Vella D., Moloney A. P., Monahan F. J. and Schmidt O. (2012) A refined sampling strategy for intra-tooth stable isotope analysis of mammalian enamel. *Geochim. Cosmochim. Acta* **84**, 1–13.

Zhang C., Wang Y., Li Q., Wang X., Deng T., Tseng Z. J., Takeuchi G. T., Xie G. and Xu Y. (2012) Diets and environments of late Cenozoic mammals in the Qaidam Basin, Tibetan Plateau: evidence from stable isotopes. *Earth Planet. Sci. Lett.* **333–334**, 70–82.

Associate editor: Miryam Bar-Matthews